Available online at www.sciencedirect.com

ScienceDirect

Procedia IUTAM 14 (2015) 321 – 328

Procedia IUTAM

www.elsevier.com/locate/procedia

IUTAM_ABCM Symposium on Laminar Turbulent Transition

Investigation of the global instability of the rotating-disk boundary layer

E. Appelquist[a,b,*], P. Schlatter[a,b], P. H. Alfredsson[a], R. J. Lingwood[a,c]

[a] *Linné FLOW Centre, KTH Mechanics, Royal Institute of Technology, SE-100 44 Stockholm, Sweden*
[b] *Swedish e-Science Research Centre (SeRC)*
[c] *University of Cambridge, Cambridge CB23 8AQ, UK*

Abstract

The development of the flow over a rotating disk is investigated by direct numerical simulations using both the linearized and fully nonlinear incompressible Navier–Stokes equations. These simulations allow investigation of the transition to turbulence of the realistic spatially-developing boundary layer. The current research aims to elucidate further the global linear stability properties of the flow, and relate these to local analysis and discussions in literature. An investigation of the nonlinear upstream (inward) influence is conducted by simulating a small azimuthal section of the disk (1/68). The simulations are initially perturbed by an impulse disturbance where, after the initial transient behaviour, both the linear and nonlinear simulations show a temporally growing upstream mode. This upstream global mode originates in the linear case close to the end of the domain, excited by an absolute instability at this downstream position. In the nonlinear case, it instead originates where the linear region ends and nonlinear harmonics enter the flow field, also where an absolute instability can be found. This upstream global mode can be shown to match a theoretical mode from local linear theory involved in the absolute instability at either the end of the domain (linear case) or where nonlinear harmonics enter the field (nonlinear case). The linear simulation grows continuously in time whereas the nonlinear simulation saturates and the transition to turbulence moves slowly upstream towards smaller radial positions asymptotically approaching a global upstream mode with zero temporal growth rate, which is estimated at a nondimensional radius of 582.

Selection and peer-review under responsibility of ABCM (Brazilian Society of Mechanical Sciences and Engineering)

Keywords: rotating disk, boundary layer flow, direct numerical simulation

1. Introduction

The incompressible boundary layer over a rotating disk without any imposed external flow is studied. The laminar profiles arising over the disk are shown in Fig. 1 and constitute the similarity solution of the cylindrical Navier–Stokes

* Corresponding author. Tel.: +46-8-790-7167
E-mail address: ellinor@mech.kth.se

Selection and peer-review under responsibility of ABCM (Brazilian Society of Mechanical Sciences and Engineering)
doi:10.1016/j.piutam.2015.03.054

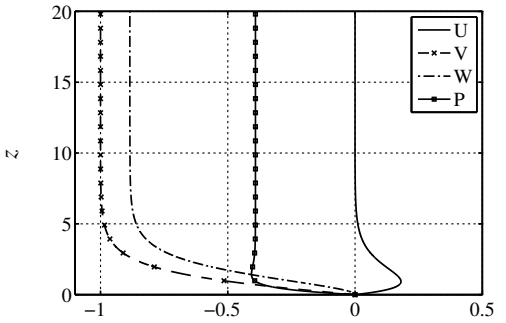

Fig. 1. The laminar velocity profiles (in the rotating reference frame) of the similarity solution for the flow over an infinite rotating disk. U is the radial velocity component, V is the azimuthal velocity component and W is the vertical velocity component. For completeness also the pressure P is included which is normalized to zero at the wall.

equations for a disk of infinite radius.[1] The boundary layer consists of a three-dimensional axisymmetric flow, with a constant thickness and a Reynolds number (R) increasing linearly with radius (r) defined by

$$R = \frac{r^*\Omega^* L^*}{\nu} = \frac{r^*}{L^*} = r, \tag{1}$$

where ν is the kinematic viscosity of the fluid, Ω^* is the rotation velocity and the nondimensionalizing lengthscale is $L^* = (\nu/\Omega^*)^{1/2}$. The star superscript refers to dimensional units where needed. The radial velocity profile ($U = U^*/(r^*\Omega^*)$) is inflectional making the flow susceptible to an inviscid crossflow instability. The stability properties have long been examined both through experiments and theory,[2,3] yet there is no clear picture of either the instability in a global frame or the precise transition mechanism eventually leading to turbulent flow.

In 1995 a local absolute instability was found to exist at a Reynolds number $R = 507$ based on theory.[3] This absolute instability appears in the local framework since it was defined by a linear stability analysis of the mean profiles at locally prescribed Reynolds numbers, ignoring the change in Reynolds number with radius. Nevertheless, this critical Reynolds number was shown to agree well with experimentally observed Reynolds numbers for the onset of nonlinearity and the subsequent transition process.[4] Thus, the discovery of the theoretical critical Reynolds number for the onset of absolute instability triggered further theoretical, experimental and numerical research.[5-8] The current research is directed towards understanding how this local concept of the absolute instability is translated to the real flow, as appearing in (real or numerical) experiments. Using experiments and model problems, both the linear and nonlinear behaviour affected by the position of the edge of the disk have been investigated.[7-9] Here, simulations including a finite extent of the linear domain are conducted, either by modelling the effect of outward turbulence (linear simulation) or with actual developed turbulence (nonlinear simulation), showing how the absolute instability behaves in its presence. The nonlinear simulation presented is used to investigate the linear behaviour in the presence of an annulus of turbulence at high R. Both simulations are part of previous work where the linear global flow was investigated.[10] For that work, the nonlinear simulation was used as a means to verify that the outer radial boundary condition for the linear domain was correctly modelling the influence of the turbulence. Here, the nonlinear simulation is described in detail and also the development in time is followed. The linear simulation is instead used as a tool to show that the behaviour uncovered remains linear. The outline is as follows. In section 2 the simulations performed are described, in section 3 the results of the simulations are shown, and in section 4 a summary and a discussion based on the results are given.

2. Simulations performed

Our simulations are performed with the massively parallel code Nek5000.[11] Nek5000 solves the incompressible Navier–Stokes equations via a Legendre polynomial-based Spectral Element Method (SEM) and is optimized for MPI-based (Message Passing Interface) usage on supercomputers.[12] The present simulations focus on the impulse

response in linear and nonlinear simulations. A polynomial order of 7 was used within the spectral elements, and the numbers of spectral elements in the simulations are 18480 (linear) and 183551 (nonlinear) and the simulations were performed on 528 and 2112 cores, respectively. The reason for the large spectral element count for the nonlinear simulation is that the small turbulent scales require a higher resolution. Also due to turbulence development, the height of the nonlinear domain was increased to $z = 49$ compared with $z = 20$ for the linear simulations. The azimuthal extent of both domains was $2\pi/68$, chosen since this azimuthal wavenumber ($\beta = 68$) is close to the critical Reynolds number $\beta = 67$ found for the absolute instability from local theory. The radial domain size is for the linear simulation $r = 400-730$ and for the nonlinear simulation $r = 400-780$. These total domain sizes differ from the actual boundary layer of interest due to a sponge region both at the inflow for small r and prior to the end of the domain for large r. The sponge was designed to damp reflections from the boundary both from the upstream mode (small r) and downstream mode (large r), forcing the flow back to the laminar von Kármán boundary layer,[10] albeit with a smaller extent for the nonlinear simulation due to lower amplitude disturbances as a result of nonlinearity. The radial extent without the sponge regions for the linear simulations was $r = 420 - 630$ and for the nonlinear simulations $r = 420 - 700$. Furthermore, a difference between the linear and nonlinear setup is that the base flow adapts for the nonlinear case. In the linear solver, the von Kármán similarity solution is set as a fixed base flow and the perturbation equations only are solved. For the nonlinear solver, the base flow is allowed to change since the full incompressible Navier–Stokes equations including the nonlinear terms are solved.

3. Simulation results

In Fig. 2 space–time diagrams show the development of an impulse disturbance excited at position $r_{ex} = 490$ in both the (a) linear and (b) nonlinear simulations. Both figures show the root mean square (rms) amplitudes of the total azimuthal velocity

$$v_{\mathrm{rms}}^2 = \frac{1}{2\pi}\int_0^{2\pi} (V - \bar{V})^2 \mathrm{d}\theta, \tag{2}$$

where V has already been normalized by the local disk velocity ($r\Omega$), and the rms values are computed at a height of $z = 1.3$. The overbar defines the azimuthal mean value. For the linear simulation in Fig. 2(a), it is possible to see the introduction of the disturbance at $r_{ex} = 490$ followed by a convectively unstable behaviour where the contours lean to the right. The time is shown as a number of complete disk rotations, *i.e.* as $T = t/(2\pi)$ where data up to $T = 4$ are included. Around $T = 1.6$, it is possible to see a change in the disturbance behaviour where the contours turn through the vertical to lean slightly to the left showing global unstable behaviour. Eventually, as the instability contaminates the whole domain, there is a positive temporal growth rate throughout. The developed flow in Fig. 2(a) shows an unstable linear global mode with a single complex global frequency ω.[10] The linear global mode is expected eventually to saturate by nonlinearity if so included in the simulation. This is clear from the space–time diagram of the nonlinear simulation, Fig. 2(b). Again the introduction of the disturbance is seen at $r_{ex} = 490$ followed by a convectively unstable behaviour. These convective disturbances obtain large amplitudes at large r and a turbulent region develops prior to the outflow sponge region ($r = 700$). Also in this simulation the behaviour turns showing globally unstable behaviour. Due to this temporally growing behaviour the turbulence is sustained and saturates further upstream with time.

The growth rates in r and t shown in Fig. 3 give a better understanding of the global mode. Shown in Fig. 3(a) is the radial growth rate at the final time for both simulations, $T = 4$ and $T = 4.5$ for the linear and nonlinear simulation, respectively. The resulting linear growth rate curve (L) corresponds well to the theoretical upstream mode α_i^- contributing to the local absolute instability at $r = 605$. The local theory line shows where two modes meet at a zero of the group velocity ($\partial\omega/\partial\alpha = 0$, where α is the radial wavenumber) for $\beta = 68$ as a function of r. Above $r = 507$ the temporal growth rate is greater than zero ($\omega_i > 0$) and the flow is locally absolutely unstable along this line. The two modes participating in the absolute instability at $r = 605$ are shown as α_i^-, the upstream mode, and α_i^+, the downstream mode. In contrast to the final behaviour from the linear simulation, the nonlinear radial growth rate at $T = 4.5$ has not yet stabilized. With time, the intersection of the nonlinear line with the local theory line moves slowly towards smaller r, this position is defined as r_{end} shown as a circle in the figure. The development in time of the nonlinear simulation can be seen more clearly in Fig. 3(b) showing both the linear (L) and nonlinear (NL) growth

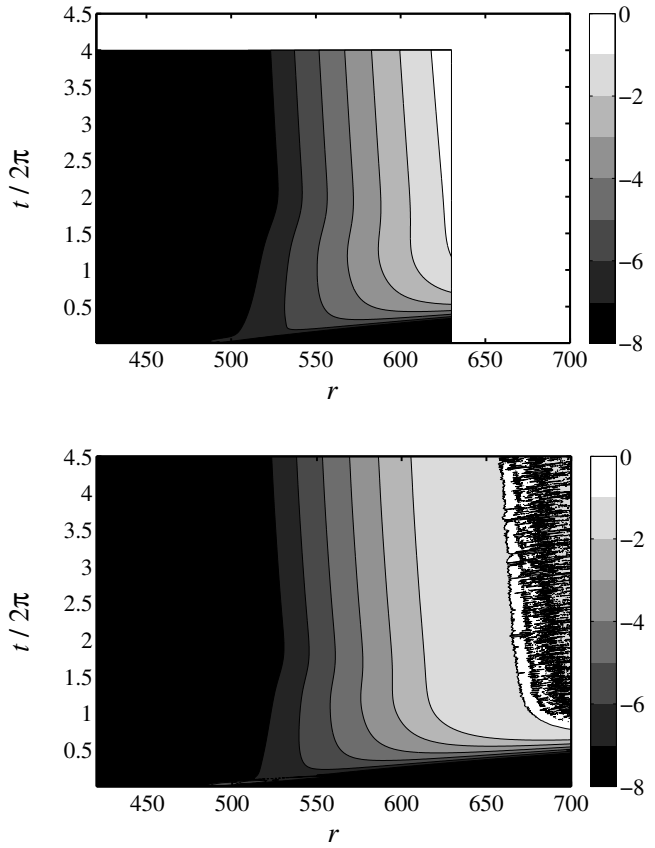

Fig. 2. Space–time diagrams showing v_{rms} at $z = 1.3$ from the: (a) linear simulation; and (b) the nonlinear simulation. Both simulations are impulsively disturbed at $r_{ex} = 490$.

rates in time at $r = 530$. While the linear simulation stabilizes for a final global growth rate of 0.070, one order lower than the theoretical growth rate of the global mode where $\omega_i = 0.707$, the nonlinear simulation does not stabilize, it continues to decay slightly. To compare the values of ω here to those normally used in local theory requires a division by r of the former. This growth rate decay of the nonlinear simulation relates both to the change of r_{end} in time and the inward motion of the turbulence. Due to the decrease of growth rate in time eventually the slow drift inwards of the turbulent front will stop as the growth rate approach zero. For both simulations the behaviour at early times is thus convective with negative temporal growth rates, changing around $T = 1.6$ (linear) and $T = 1.5$ (nonlinear), both resulting in global growth. Also, the temporal global frequency of the theoretical mode, $\omega_r = -15.0$ (in the rotating reference frame), is comparable to the global mode in the linear simulation where the frequency found is -14.6.

The slow inward motion of the global mode present in the nonlinear simulation is illustrated in Fig. 4 where three snapshots are shown at $z = 1.3$. The times of these snapshots are $T = 2.5$, 3.5 and 4.5, where the logarithms of the total azimuthal velocities (not normalized by the rotation of the disk, $r\Omega$) are shown. The thick dashed lines indicate r_{end}, where the radial growth rate is equal to the absolute instability found in local theory, *i.e.* the radial position where the upstream mode is part of an absolute instbility, see Fig. 3(a). However, the phase shift in the visualized waves between the single revolutions is not only due to the movement of r_{end} towards smaller r in time, it is also due to the fact that the waves are travelling with respect to the disk, *i.e.* ω_r is nonzero. For $T = 4.5$, $r_{end} is 591$, indicated as a thick dashed line in Fig. 5 showing the energy of the nonlinear azimuthal modes extracted via Fourier transforms, E_β, as a function of r. The position r_{end} is shown to approximate to the position where the difference between the

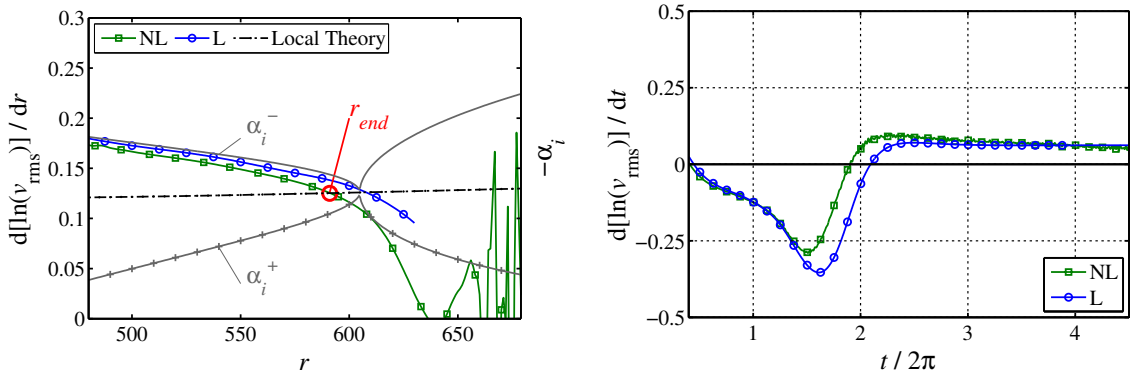

Fig. 3. Growth rates in space and time of $v_{\rm rms}$ at $z = 1.3$. (a) d[ln($v_{\rm rms}$)]/dr for the linear (L) and nonlinear (NL) simulations. The local theory line for zero group velocity at $r = 605$ and $\beta = 68$ is also shown, along which the absolute instability occurs above $r = 507$ (where $\omega_i > 0$). The modes participating in the absolute instability at $r = 605$ are shown both for the upstream mode, α_i^-, and the downstream mode, α_i^+. The intersection of the NL line and local theory line is indicated by r_{end} in the figure. (b) d[ln($v_{\rm rms}$)]/dt for the linear (L) and nonlinear (NL) simulations taken at $r = 530$. The L line is extrapolated to $T = 4.5$.

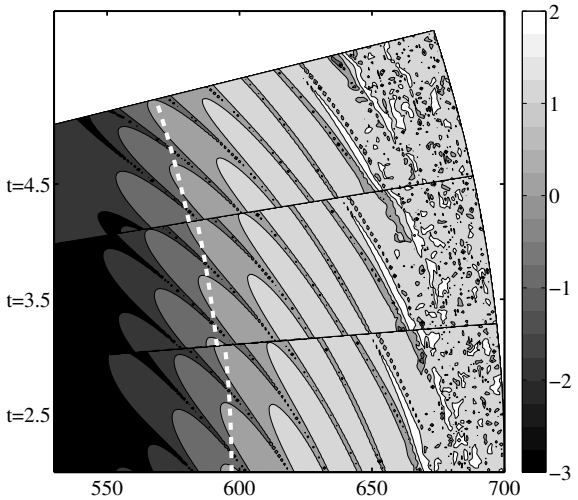

Fig. 4. Three snapshots from the nonlinear simulation at times $T = 2.5$, 3.5 and 4.5 (a difference of one revolution each) of the total azimuthal velocities (not normalized by the rotation of the disk, $r\Omega$) at $z = 1.3$. The velocities are shown in logarithmic scale. The thick dashed line indicates r_{end} defined as the location where the upstream mode matches the absolute instability from local theory.

fundamental mode and its first harmonic is 5 orders of magnitude. This position is thus in a region separating the linear and nonlinear behaviour.

Due to the slow drift of r_{end} upstream with time, the excited linear global mode is decreasing with time and eventually the motion will stop as the growth rate reaches zero. The linear global mode within the nonlinear simulation thus asymptotically moves towards a global mode of zero growth rate in time, seen in Fig. 3(b). This steady state can be approximated by comparing the growth rates in time to the position of r_{end} as seen in Fig. 6. The linear simulation is shown as a marker since this simulation reaches a steady growth rate in time and only has one value of r_{end}. The nonlinear simulation is shown as a thick line for $T = 2.5 - 4.5$ to the left of the linear marker. Also the direction of time, T, is shown for the nonlinear line. A linear fit is made to the nonlinear line such that the asymptotic position for $T \to \infty$ can be estimated. This value is taken where the fitted curve crosses the zero line, such that the approximated

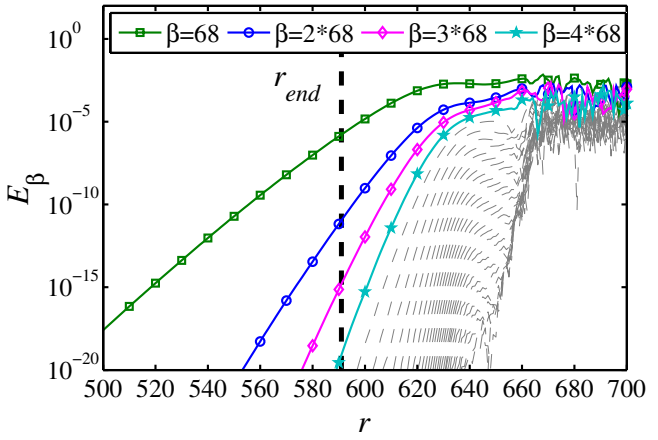

Fig. 5. The energy content of the nonlinear azimuthal modes extracted via Fourier transforms. The position of r_{end} (thick dashed red line) estimates the boundary between the linear and nonlinear behaviour of the flow field.

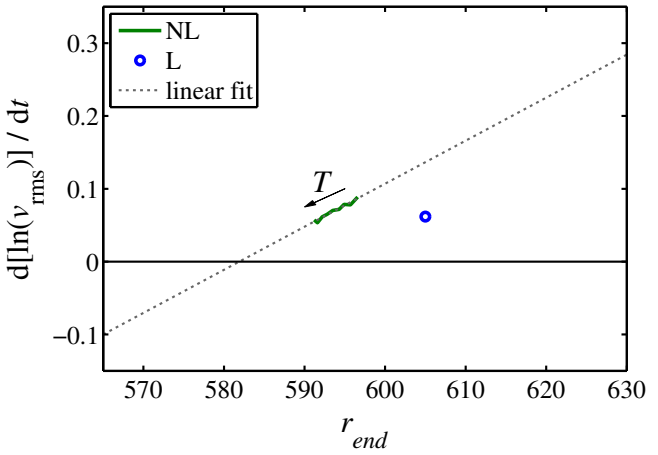

Fig. 6. Growth rates in time as a function of r_{end}. The final growth rate ($T = 4$) of the linear simulation (L) and from the nonlinear simulation (NL) growth rates between $T = 2.5 - 4.5$ are shown. T indicates the direction of time in the nonlinear simulation. A linear fitted curve on the nonlinear data is also included, along with the zero line.

position of r_{end} is 582. The difference between the r_{end} position in the linear and nonlinear simulations, where the growth rate in t is the same, is possibly due to the downstream linear–nonlinear difference. In Fig. 7 (which is adapted from figure 12(a) in Ref. 13) experimental data is shown with the r_{end} position included as a dashed line. Also the breakdown position just prior to turbulence, where the v_{rms} reaches its maximum value (not shown herein) is included as a solid line from the nonlinear simulation. Further simulations both including the stationary vortices and the global linear mode are needed to make a quantitative comparison to experiments.

4. Summary and discussion

The *linear* behaviour of an impulse disturbance has been investigated in both a linear and a nonlinear simulation. Similar linear upstream modes are found matching those of linear local theory. The nonlinear simulation successfully shows the influence of the nonlinear turbulent region on the upstream flow, adjusting the linear mode to have zero growth rate creating an asymptotically stationary behaviour separating the linear and nonlinear domain at $r_{end} = 582$.

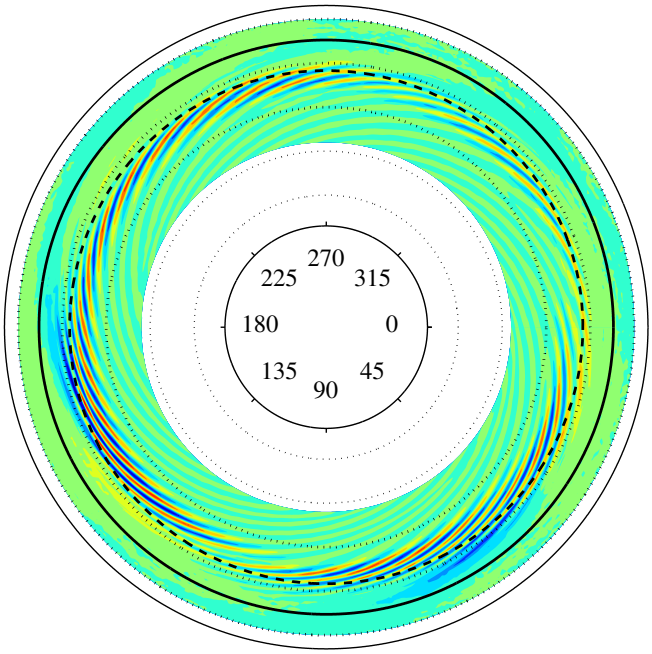

Fig. 7. Experimental data from figure 12(a)[13] showing ensemble-averaged azimuthal fluctuation velocities measured at $z = 1.3$, where $r_{end} = 582$ for the asymptotic state is included as a dashed line. Also the breakdown position just prior to turbulence, where the v_{rms} reaches its maximum value (not shown) is included as a solid line from the nonlinear simulation. The disk is rotating anti-clockwise.

This linear behaviour of an impulse disturbance has previously been investigated in DNS[5] both locally and globally. The local behaviour concurred with the findings of the absolute instability by Lingwood (1995).[3] The global linear behaviour, however, was previously shown to be convectively unstable, rather than absolute, when the edge is assumed to be at an infinite distance. When using boundary conditions that do not interact with the flow in any way, there is no generation of the upstream mode creating a globally unstable flow, with disturbances that are fundamental to the absolute-instability mechanism.[3] Our turbulent region, or in the linear case our sponge region, shows that the flow changes nature from being convectively unstable to absolutely unstable. It is important to realize that the findings for a linear *infinite* disk[5] are still valid. Previous results when an outer boundary condition is included in a global linear stability analysis have shown to result in a linearly globally unstable flow — at least in the model problem using the linear Ginzburg–Landau equation.[7] These results correspond to ours, with a slight difference in the sense that Healey's[7] outer radial boundary condition links the edge of the disk to the generation of the inward travelling modes, while our outer radial boundary condition links to the end of the linear domain, where the flow starts its transition to turbulence. The analysis here of the nonlinear simulation where turbulence is present creates a link to the real boundary layer. The experimental data in Fig. 7 also show the DNS positions of both r_{end} and where the flow breaks down to turbulence. However, for the real physical boundary layer the convectively-unstable stationary vortices excited by stationary roughnesses on the disk surface are unavoidable and simulations with stationary roughnesses are expected to give a further link to experimental results.

Thus, we can summarize that the rotating-disk boundary layer is globally linearly stable when it has an infinite radius,[5] and globally linearly unstable when influenced by an outer annulus of turbulence. However, the global linear stability of the infinite disk cannot be sustained in reality, where the convective radial growth (due to *e.g.* roughness) would eventually result in a turbulent patch, which in turn creates an upstream global mode. This front will eventually move inwards, and settle down at an estimated radial position of $r_{end} = 582$.

Acknowledgements

This work is supported by the Swedish Research Council through the ASTRID project and the Linné FLOW Centre. Computer time is provided by SNIC (Swedish National Infrastructure for Computing). Fruitful discussions with Shintaro Imayama are also gratefully acknowledged.

References

1. von Kármán, T. Über laminare und turbulente Reibung. *Z Angew Math Mech* 1921;**1**:232–252.
2. Wilkinson, S, Malik, MR. Stability experiments in the flow over a rotating disk. *AIAA J* 1985;**23**:588–595.
3. Lingwood, RJ. Absolute instability of the boundary layer on a rotating disk. *J Fluid Mech* 1995;**299**:17–33.
4. Lingwood, RJ. An experimental study of absolute instability of the rotating-disk boundary-layer flow. *J Fluid Mech* 1996;**314**:373–405.
5. Davies, C, Carpenter, PW. Global behaviour corresponding to the absolute instability of the rotating-disc boundary layer. *J Fluid Mech* 2003;**486**:287–329.
6. Pier, B. Finite-amplitude crossflow vortices, secondary instability and transition in the rotating-disk boundary layer. *J Fluid Mech* 2003; **487**:315–343.
7. Healey, JJ. Model for unstable global modes in the rotating-disk boundary layer. *J Fluid Mech* 2010;**663**:148–159.
8. Imayama, S, Alfredsson, PH, Lingwood, RJ. An experimental study of edge effects on rotating-disk transition. *J Fluid Mech* 2013; **716**:638–657.
9. Pier, B. Transition near the edge of a rotating disk. *J Fluid Mech* 2013;**737**:R1.
10. Appelquist, E, Schlatter, P, Alfredsson, PH, Lingwood, RJ. Global linear instability and the radial boundary of the rotating-disk flow. *J Fluid Mech* 2014;(submitted).
11. Fischer, PF, Lottes, JW, Kerkemeier, SG. Nek5000. *Web page http://nek5000mcsanlgov* 2012;.
12. Tufo, HM, Fischer, PF. Fast parallel direct solvers for coarse grid problems. *J Parallel Distrib Comput* 2001;**61**(2):151–177.
13. Imayama, S, Alfredsson, PH, Lingwood, RJ. On the laminar-turbulent transition of the rotating-disk flow – the role of absolute instability. *J Fluid Mech* 2014;**745**:132–163.